Geophysical Research Letters

RESEARCH LETTER
10.1029/2022GL099998

Key Points:

- Current methods used to calculate Madden-Julian oscillation (MJO) indices result in degeneracy and unphysical oscillatory behavior
- A simple projection and rotation algorithm is derived as a postprocessing step to current MJO index calculations
- Adding a simple rotation results in a slowly varying index basis that retains the broad structure of the original index

Supporting Information:

Supporting Information may be found in the online version of this article.

Correspondence to:

S. Weidman,
sweidman@g.harvard.edu

Citation:

Weidman, S., Kleiner, N., & Kuang, Z. (2022). A rotation procedure to improve seasonally varying empirical orthogonal function bases for MJO indices. *Geophysical Research Letters*, *49*, e2022GL099998. https://doi.org/10.1029/2022GL099998

Received 9 JUN 2022
Accepted 18 JUL 2022

A Rotation Procedure to Improve Seasonally Varying Empirical Orthogonal Function Bases for MJO Indices

Sarah Weidman[1], Ned Kleiner[1], and Zhiming Kuang[1,2]

[1]Department of Earth and Planetary Sciences, Harvard University, Cambridge, MA, USA, [2]John A. Paulson School of Engineering and Applied Sciences, Harvard University, Cambridge, MA, USA

Abstract Various indices have been defined to characterize the phase and amplitude of the Madden-Julian oscillation (MJO). One widely used index is the outgoing longwave radiation (OLR) based MJO index (OMI), which is calculated using the spatial pattern of 30–96-day eastward-filtered OLR. The empirical orthogonal functions (EOFs) used to calculate the OMI in observations are prone to degeneracy and exhibit oscillations on the order of 10–20 days, despite initial filtering of the OLR. We propose a simple modification to the OMI that involves aligning the EOFs between neighboring days while retaining the spatial pattern described by the EOFs. This rotation method is implemented as a postprocessing procedure of the current OMI calculation and cleanly removes the spurious oscillations and degeneracy issues seen in the standard method. A similar rotation procedure can be implemented in calculations of other MJO indices.

Plain Language Summary Characterization of the Madden-Julian oscillation (MJO) is important for subseasonal weather forecasting. However, the indices often used to characterize the MJO are projected onto a basis that includes unphysical day-to-day variations and noise that arise from the mathematical procedure used to calculate the basis, rather than the atmosphere itself. We propose a modified postprocessing procedure to the standard method that removes spurious oscillations in the index basis while maintaining the broad structures of the original index.

1. Introduction

The Madden-Julian oscillation (MJO) is characterized by eastward propagating convection anomalies in the Indian and Pacific tropical oceans with a period of 30–60 days (Madden & Julian, 1971, 1972). In addition to being a dominant intraseasonal variability in the tropics, the state of the MJO has also been connected to weather at higher latitudes (e.g., Arcodia et al., 2020; Henderson et al., 2016), among many other aspects of global atmospheric circulation. Reviews on the significance of the MJO appear in Jiang et al. (2020) and Zhang (2005).

The influence of the MJO on the global climate system is dependent on the spatial pattern and amplitude of the MJO signal, which are often quantified using an index generated by empirical orthogonal functions (EOFs). The phase of the MJO, based on these indices, is used to predict or otherwise characterize the influence of the MJO on various atmospheric phenomena (J. Wang et al., 2020). One frequently used index is the real-time multivariate (RMM) index (M. C. Wheeler & Hendon, 2004). The RMM is based on the zonal structure of OLR and zonal wind at 200 and 850 hPa, and can be used for real-time monitoring of the MJO. However, Straub (2013) showed that the RMM underrepresents convection compared to zonal wind, causing the RMM to miss some MJO-like convective signals. In addition, the lack of meridional structure confounds the MJO signal with equatorial Kelvin waves (Roundy et al., 2009).

An OLR-based MJO index (OMI) was developed to counteract some of these issues, since it incorporates the zonal and meridional structure of OLR into a pair of propagating EOFs over the course of the year (Kiladis et al., 2014) (hereafter K14). Incorporation of meridional structure helps separate the MJO signal from Kelvin waves, and using solely OLR more directly tracks the convective signal. Since OLR can be measured directly by satellites, the OMI provides a reliable long-term record of tropical convective patterns (S. Wang, 2019).

Due to these benefits, the OMI is a widespread index used for MJO analyses. However, there remain a few small but important issues with the original OMI. Since the EOFs of the OMI represent propagating waves of the MJO, the leading EOF pair are of a similar magnitude (North et al., 1982), resulting in a somewhat arbitrary choice when assigning the EOFs as EOF1 or EOF2. In the original OMI calculation, the leading pair of eigenvalues

become degenerate in early November, which K14 resolves by linearly interpolating the EOFs between November 1 and November 8. Further, the direction of the EOFs varies from day-to-day, resulting in noise that does not reflect variation in a physical MJO signal (S. Wang, 2019). These issues are more pronounced when using shorter duration datasets, such as may be required when evaluating model output.

In the past few years, new MJO indices have been developed to reduce noise by rotating the EOFs. S. Wang (2019) built upon the OMI by including precipitation and rotating the EOFs to align the center of convection in the Indian Ocean. S. Wang et al. (2022) rotated a set of EOFs derived from both OLR and wind (as in the RMM) to align the 850 hPa zonal wind between neighboring days, with a different rotation amount each day.

In this paper, we derive a rotation algorithm that can be incorporated into the original OMI calculation as a post-processing procedure. The amount of rotation is based on a mathematical alignment of the EOFs between neighboring days, largely eliminating the need for arbitrary choices seen in previous methods. The simple rotation reduces noisiness in the OMI and removes the need for interpolation due to EOF degeneracy, while maintaining the same eigenvalues and general EOF structure as the original OMI. A derivation of the rotation algorithm is described in Section 2. An analysis of the resulting EOFs and principal components (PCs) of the new index compared to the original OMI is shown in Section 3. A discussion follows in Section 4.

2. Methods

2.1. Data

Analyses of the OMI were performed using the interpolated OLR data set provided by NOAA/OAR/ESRL PSL, Boulder, Colorado, USA (Liebmann & Smith, 1996), as used in the original OMI calculation in K14. To compare EOFs directly to the original paper, EOFs are derived from the period 1979–2012, but the procedure can be repeated with differing time periods. Implementation of the original OMI index was performed using the Python package published in Hoffmann et al. (2021). The rotation method derived in this paper acts as an additional post-processing step to the same package.

2.2. Derivation of Rotation Algorithm

The derivation of the original OMI is described in detail in K14. We briefly summarize their steps here:

1. Daily OLR between 20°S and 20°N is filtered using a 30–96-day, eastward-only bandpass filter, following M. Wheeler and Kiladis (1999).
2. EOFs for each day of year (DOY) are calculated from the filtered OLR data set, using data from all years within a 121-day window centered at the respective DOY.
3. Arbitrary sign reversals between EOFs from neighboring DOYs are removed by a sign flip to maintain continuity across days.

These steps result in a set of 366 EOF pairs, one pair for each day of year. Intricacies regarding leap years are discussed in Hoffmann et al. (2021). The teal lines in Figure 1 show the angle between the EOF vector at each DOY and the EOF vector on DOY 1 (January 1) using the original OMI algorithm. The angle between EOFs is used here to describe day-to-day variations within the EOF basis. Although the OLR is filtered to remove any signals faster than 30 days, high frequency oscillations of the angles between EOFs are notable near the beginning and end of the year. In these analyses, we have not interpolated the EOFs in early November (DOY 293–316) to remove issues due to degeneracy, as was done in K14. Interpolation smooths the largest spike near DOY 300 but is otherwise unchanged.

As described in S. Wang (2019) and S. Wang et al. (2022), adding an orthogonal rotation to the EOFs can remove some of the high-frequency noise while maintaining the overall EOF structure. The first two EOFs explain similar amounts of variance throughout the year (see: K14), as is characteristic of the EOFs of a propagating signal (Wilks, 2019). Because the pair of EOFs are approximately degenerate, the direction that the two orthogonal vectors point within the plane defined by the leading EOF pair is sensitive to sampling errors and hence arbitrary (North et al., 1982).

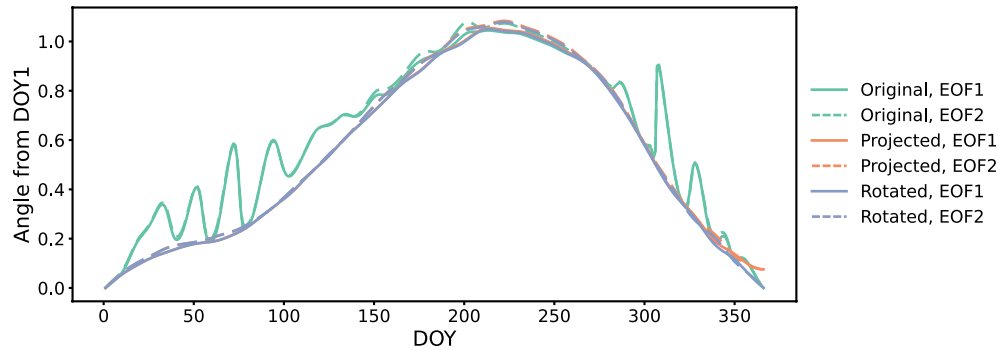

Figure 1. Angle between the empirical orthogonal function (EOF) vector at day of year 1 (January 1) and each day of year. Solid lines are the angles for EOF1 and dashed lines for EOF2. Original (teal) EOFs are the same as calculated in K14, without the interpolation in November. Projected (orange) EOFs are rotated by Equation 4. Rotated (purple) EOFs are rotated by Equation 6.

We address these issues by rotating the first two EOFs for each day to align with the EOFs of the previous day, within the 2-D plane defined by the original EOF vectors. To determine the required rotation, we first define a matrix $\mathbf{E}_j$ with columns corresponding to the first two EOFs of some DOY j (e.g., for January 1, $j = 1$):

$$\mathbf{E}_j = \left[\overrightarrow{\text{EOF}1}_j \quad \overrightarrow{\text{EOF}2}_j\right] \tag{1}$$

$\mathbf{E}_{j-1}$ is defined similarly from the EOFs on day $j - 1$. We want the rotated EOFs on day j to align with the EOFs of the previous day, but within the plane defined by the original EOFs, $\mathbf{E}_j$. This can be achieved by projecting the EOFs from the previous day onto $\mathbf{E}_j$. The projection of $\mathbf{E}_{j-1}$ onto $\mathbf{E}_j$ is

$$\hat{\mathbf{E}}_j = \mathbf{E}_j\left(\mathbf{E}_j^T\mathbf{E}_j\right)^{-1}\mathbf{E}_j^T\mathbf{E}_{j-1} \tag{2}$$

where $\mathbf{E}^T$ is the transpose matrix and $\hat{\mathbf{E}}$ is the projected matrix. Since the EOFs are orthonormal, this reduces to:

$$\hat{\mathbf{E}}_j = \mathbf{E}_j\mathbf{E}_j^T\mathbf{E}_{j-1} \tag{3}$$

The projection in Equation 3 is repeated for each DOY using the rotated EOF matrix from the previous day to project onto the plane defined by the subsequent day's original EOFs:

$$\hat{\mathbf{E}}_j = \mathbf{E}_j\mathbf{E}_j^T\hat{\mathbf{E}}_{j-1} \tag{4}$$

The resulting set of projected EOFs are then renormalized to unit length. The maximum change in amplitude of the EOFs after projection is of order 10^{-3}, so the renormalization step does not significantly change the projected EOFs. Since the EOFs are orthonormal, orthogonality is preserved after projection.

The angle between the projected EOFs on each DOY from the EOFs on January 1 are plotted in orange in Figure 1. The projection in Equation 4 removes the higher frequency oscillations in the original EOFs. However, this method does not guarantee that the EOFs are continuous through December 31 to January 1.

In order to maintain continuity of the EOFs across December to January, we add an extra rotation to guarantee that projecting the rotated EOFs from December 31 onto January 1 returns the original EOFs from January 1. An extra rotation by some constant angle δ is defined by the rotation matrix $\mathbf{R}$:

$$\mathbf{R} = \begin{bmatrix} \cos\delta & -\sin\delta \\ \sin\delta & \cos\delta \end{bmatrix} \tag{5}$$

This rotation amends Equation 4 to:

$$\hat{\mathbf{E}}_j = \mathbf{E}_j\mathbf{E}_j^T\hat{\mathbf{E}}_{j-1}\mathbf{R} \tag{6}$$

Intuitively, it may be clear that the EOFs on each day should be rotated by a δ that is 1/366 (to account for leap years) of the discontinuity between December 31 and January 1, essentially splitting the discontinuity equally between each day. This assumption is justified using a recursive relationship. We continue the procedure in Equation 6 to day $j + 1$:

$$\hat{\mathbf{E}}_{j+1} = \mathbf{E}_{j+1}\mathbf{E}_{j+1}^{T}\hat{\mathbf{E}}_{j}\mathbf{R} \tag{7}$$

Substituting in Equation 6 for $\hat{\mathbf{E}}_j$:

$$\hat{\mathbf{E}}_{j+1} = \mathbf{E}_{j+1}\mathbf{E}_{j+1}^{T}\mathbf{E}_{j}\mathbf{E}_{j}^{T}\hat{\mathbf{E}}_{j-1}\mathbf{R}\mathbf{R} \tag{8}$$

Continuing for each day of the year gives:

$$\hat{\mathbf{E}}_{j+m} = \prod_{k=j}^{j+m}\left(\mathbf{E}_{k}\mathbf{E}_{k}^{T}\right)\hat{\mathbf{E}}_{j-1}\mathbf{R}^{m} \tag{9}$$

Following this projection and rotation for $m = 366$ days will result in a pair of EOFs for day j that are offset from the original EOFs by $\mathbf{R}^m$. This angular distance is the discontinuity seen in Figure 1. To guarantee that the EOFs return to their original position after 1 year of rotation, we choose δ to be the negative of the discontinuity between the original EOFs on January 1, and the EOFs on January 1 after a year of projections, divided by the number of days in a year. The discontinuity is the same for both EOF1 and EOF2. Essentially we are unwinding the discontinuity resulting from Equation 4 by a small rotation each day. The only assumption made is that the rotation represented by $\mathbf{R}$ is spread uniformly across the year, which is a rather mild assumption. The resulting rotated EOFs are renormalized to unit length.

In standard EOF rotations, the rotated EOFs lose either or both of the properties that the EOFs are orthogonal and uncorrelated (Jolliffe, 1995; Wilks, 2019). However, as in S. Wang (2019), since only the degenerate pair of EOFs is rotated, rather than an empirically chosen number of EOFs, this limitation is avoided. Since the rotation matrices in Equation 6 are orthonormal, orthogonality is preserved. The resulting variance explained by the rotated EOFs is identical to the original EOFs (not shown).

3. Results

The angle from January 1 of the EOFs rotated by Equation 6 are shown in purple in Figure 1, corresponding to a δ of -0.0002 (radians). The projection and rotation is able to eliminate high frequency oscillations and maintain continuity between December 31 and January 1. The broad shape of the EOF time series of the original index is preserved.

The large-scale structure of the EOFs throughout the year is largely unchanged. Figure 2a shows spatial maps of EOF1 and EOF2 for January 15 and July 15, similar to Figure 2 of K14. The original EOFs are calculated using the same method as in K14. The spatial pattern of the original EOFs and the rotated EOFs are similar, suggesting that the basic structure of the EOFs are preserved after rotation through both winter and summer. The correlation between the original and rotated EOFs for each DOY are shown in Figure 2b. The correlations for EOF1 and EOF2 are nearly identical. The mean correlation is 0.97 for both EOFs, and the minimum correlation is 0.69 on DOY 308, when the original EOFs are degenerate (see K14).

The effect of rotation is better shown by changes in spatial structure of the EOFs over time. Figure 3 shows spatial maps of EOF1 for every other day in November. For visual clarity, the November mean EOF1 at each grid point has been removed. A similar figure for EOF2 can be found in the supplement. The original EOFs are not interpolated in early November as was done in K14 to highlight the effect of degeneracy in the original EOFs. This is clearly seen in the first two rows: the original EOF1 on DOY 305 has the same structure as EOF2 for the rest of the month (see Figure S2 in Supporting Information S1), before switching back to EOF1 on DOY 307. The rotated EOFs avoid this issue.

Beyond the degeneracy on DOY 305, the amplitude of the unrotated EOFs varies approximately every 10 days, compared to the slowly varying rotated EOFs. Because OLR is first filtered to retain only signals between 30 and 96 days, the higher-frequency variations in the original EOFs do not represent a physical signal. A movie of the

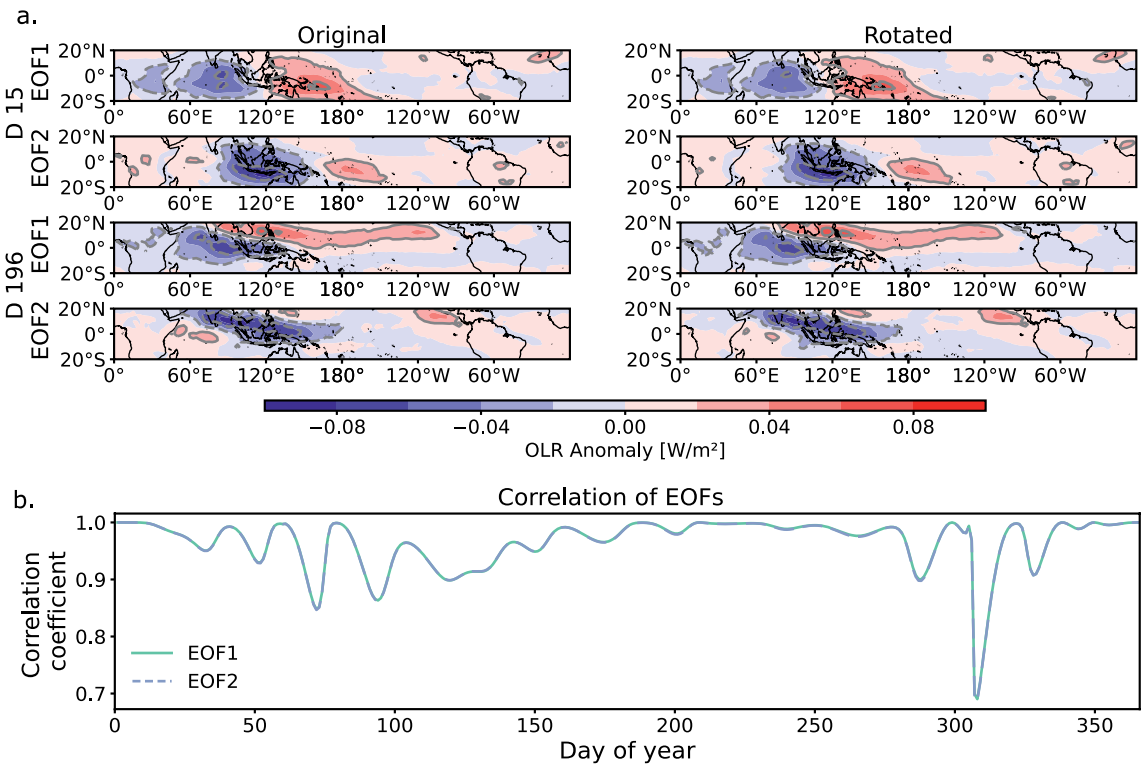

Figure 2. (a) Projections of empirical orthogonal function (EOF1) and EOF2 for January 15 and July 15. Original (left) EOFs are calculated using the method in K14. Rotated (right) EOFs are rotated by Equation 6. Gray contours are every 0.04 W m^{-2}. (b) Correlation between original and rotated EOFs for each day of year.

spatial variations in both EOFs throughout the year can be found in the Supplementary Movie S1, showing rapid oscillations of EOF structure in the original EOFs compared to the slowly varying rotated EOFs.

Using the EOF basis, the strength and phase of the MJO is determined by projecting observed daily OLR onto the EOF pair of the corresponding DOY, resulting in a pair of principal components (PCs). The method used here to calculate the PCs is identical to that described in K14, but using the rotated EOFs as the basis. As in K14, daily OLR is filtered to include 20–96-day frequencies and all eastward- and westward-propagating wavenumbers and then projected onto the corresponding EOF pair for that DOY. The PCs are then normalized so PC1 has a standard deviation of one.

A time series of the two PCs of the original OMI and the PCs projected onto the rotated EOFs are shown in Figure 4. The time series is plotted for 2011 to compare with Hoffmann et al. (2021), and the PCs are normalized using the full 1979–2012 time period. In general, the PCs from the rotated index preserve the basic structure of the original OMI, with deviations in spring and fall months where the oscillatory behavior of the original EOFs is most pronounced. The correlation between the original and rotated index is 0.97 for PC1 and 0.95 for PC2 for this time period. The original PCs have not been interpolated in early November to avoid degeneracy, but interpolation does not substantially change the results.

The amplitude of the PCs are often plotted on a phase diagram to track MJO phase and propagation. Three-month phase diagrams for the winter of 2011–2012 for the original OMI and the rotated case are plotted in Figure 5. The axes are chosen using the convention of RMM phase diagrams, since OMI(PC2) is analogous to RMM(PC1) and -OMI(PC1) is analogous to RMM(PC2). The 2011–2012 winter is used to compare to the case study shown in K14, which classified MJO events using the index and observations from the DYNAMO field experiment in October 2011–March 2012 (Gottschalck et al., 2013; Johnson & Ciesielski, 2013; Yoneyama et al., 2013). An MJO signal is characterized by counterclockwise (eastward) motion with an amplitude larger than one.

Broadly, the phase diagrams are similar between the original OMI and the rotated case, except that kinks in the original OMI are removed by rotation. The DYNAMO campaign observed two shorter MJO events in October and November, and one longer-term MJO event in February and March. As described in K14, the OMI reasonably

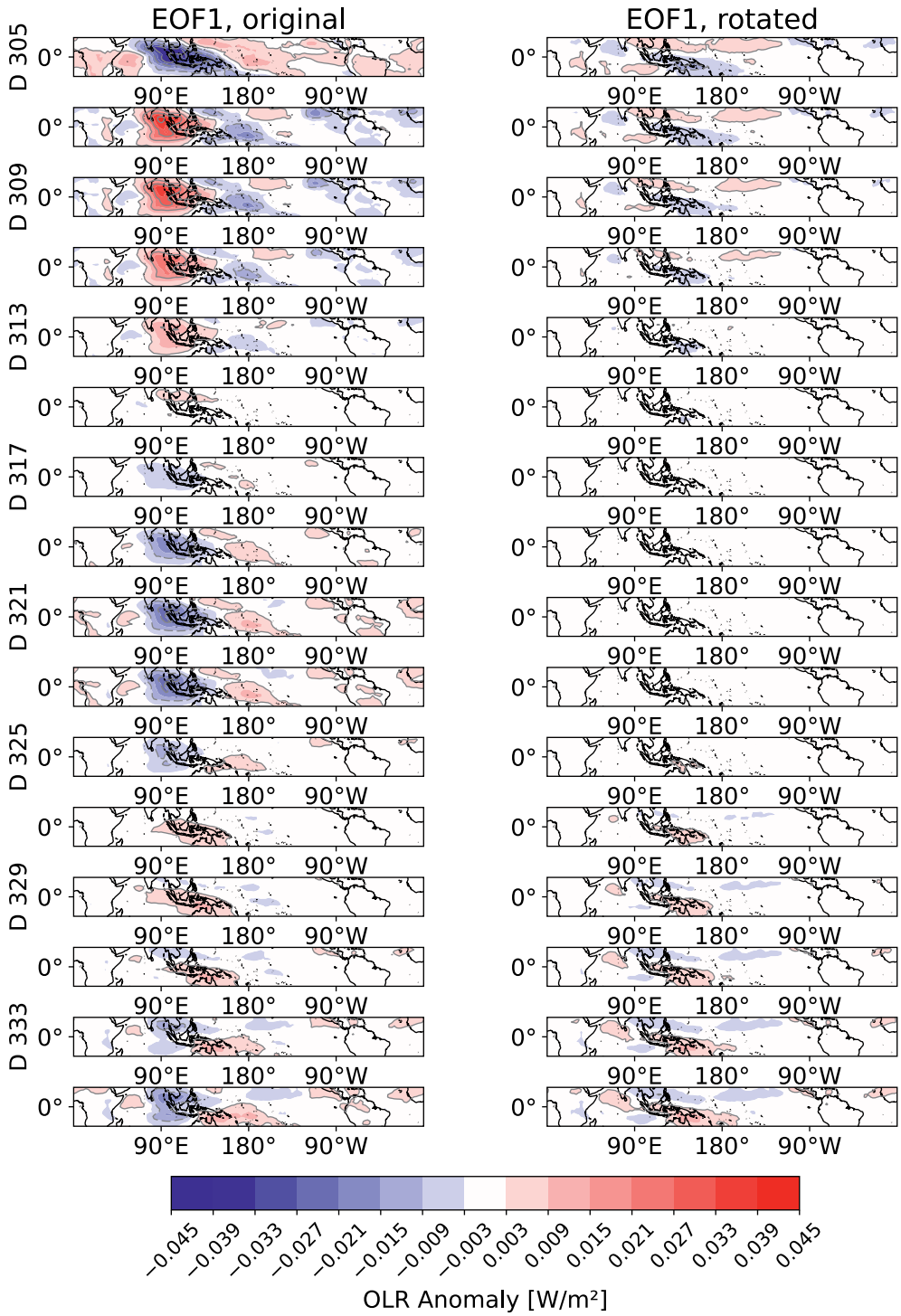

Figure 3. Projections of empirical orthogonal function (EOF1) with the November mean removed for every other day in November. Original (left) EOFs are calculated using the method in K14, without the interpolation step. Rotated (right) EOFs are rotated by Equation 6. Gray contours are every 0.012 W m^{-2}. A similar plot for EOF2 is shown in Figure S2 in Supporting Information S1.

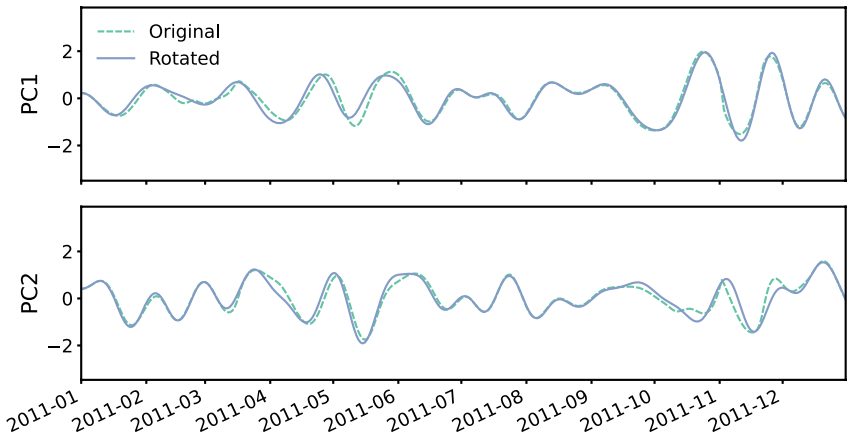

Figure 4. Daily time series of PC1 and PC2 in 2011. Dashed teal lines are calculated using the empirical orthogonal functions (EOFs) in K14. Solid purple lines are calculated using EOFs rotated by Equation 6.

represents these events in the phase diagram, and the rotated version captures the same events with similar timing. The MJO in October is seemingly better represented by the rotated case, since the kink in the original OMI has been smoothed by rotation. K14 used another case study from the winter of 2009–2010; phase diagrams from this period are plotted in Figure S3 in Supporting Information S1.

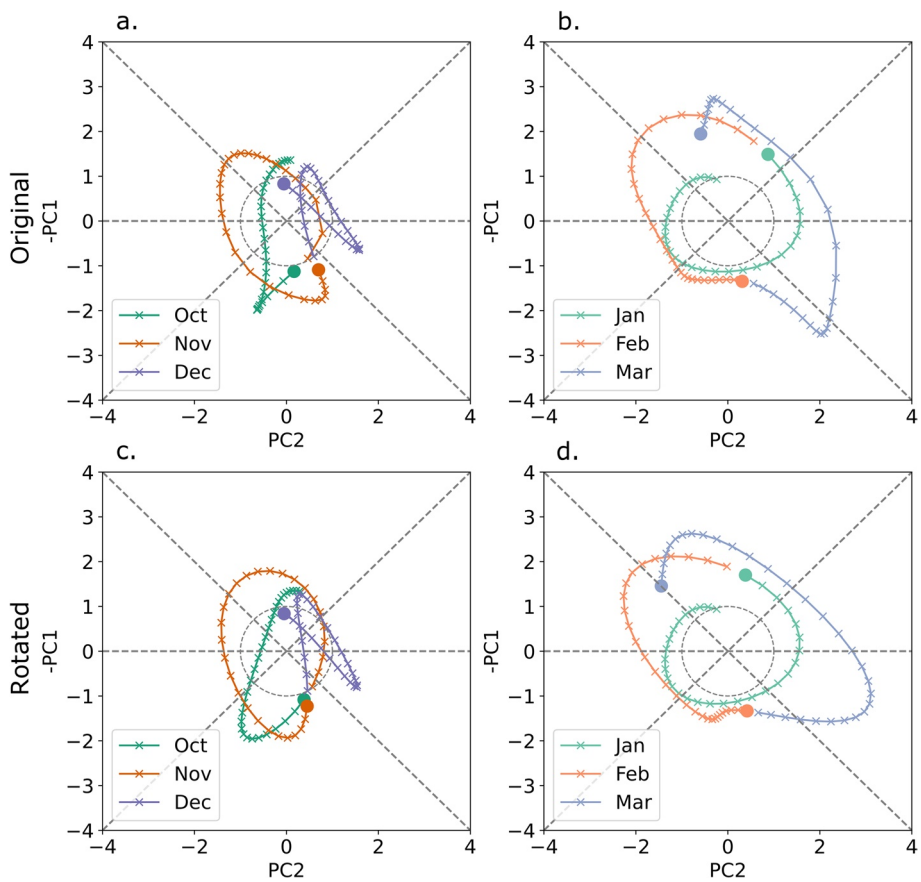

Figure 5. Three-month phase diagrams of the PCs for the 2011–2012 winter season, with October-December on the left and January-March on the right. Solid dots signify the end of each month. Top panels are calculated using the procedure in K14. Bottom panels are calculated using empirical orthogonal functions rotated by Equation 6. The dashed gray circle has a radius of 1. Figure S3 in Supporting Information S1 is a similar figure for the 2009–2010 season.

4. Discussion

By introducing a simple orthogonal rotation to the EOF basis of the original OMI described in K14, we developed a modified OMI that removes spurious high-frequency oscillations in the EOF basis while maintaining the overall structure of the original index. The rotated EOF basis varies more slowly over the course of the year, as would be expected by a basis that follows climatology. The resulting PCs preserve the same broad structure as the original OMI but remove kinks in the index. Because the rotated index closely tracks the original OMI, using the rotated index will not largely change scientific results found using the widespread OMI. However, the rotated index provides assurance that any propagating signals described by the PCs are due to a physical atmospheric event, rather than noise inherent to the EOF calculation.

The MJO community has developed a number of indices that are useful for varying purposes. Rather than introducing another index to the field, we propose this rotation method as a post-processing procedure for any EOF-derived indices to reduce noise in the index. Other new indices have already used an orthogonal rotation to reduce noise in the calculation of their EOFs (S. Wang, 2019; S. Wang et al., 2022). Our main contribution here is a rotation procedure that is based on mathematical alignment of the EOFs between neighboring days and a small constant-in-time adjustment to maintain continuity throughout the year. This procedure thus eliminates the need for arbitrary choices in previous rotation procedures, and is arguably more elegant.

The rotation described in this paper could also be useful for improving the robustness of indices limited by data availability. Shorter duration datasets are inherently noisier, which could result in unrealistic results. For example, when using a 20-year subset of OLR data to calculate the EOFs, the original OMI calculation results in a 180° discontinuity between January 1 and December 31, making it difficult to track MJO propagation throughout the winter. As shown in Figure S1 in Supporting Information S1, rotating the EOFs removes noise and guarantees continuity across December 31 to January 1.

As the open source MJO analysis software published by Hoffmann et al. (2021) was critical to this enhancement to the OMI, we hope that future researchers will be able to utilize this method in a similar manner. A Python library with the rotation post-processing procedure is currently publicly available. It can be used as an additional component to the OMI package released by Hoffmann et al. (2021) or added to calculations of other EOF-based MJO indices.

Conflict of Interest

The authors declare no conflicts of interest relevant to this study.

Data Availability Statement

Interpolated daily OLR data provided by the NOAA/OAR/ESRL PSL, Boulder, Colorado, USA, from their Web site at https://psl.noaa.gov/data/gridded/data.olrcdr.interp.html. The open source mjoindices Python package used to calculate the original OMI was published by Hoffmann et al. (2021). Python code for the projection and rotation of the EOFs is currently available at https://doi.org/10.5281/zenodo.6870694 as an addition to the mjoindices package published by Hoffmann et al. (2021). We expect that the full method will be available directly in the mjoindices package in the near future.

Acknowledgments
We thank two anonymous reviewers for their valuable feedback on the manuscript. S. W. was supported by the Harvard Graduate School of Arts and Sciences. N. K. and Z. K. were supported by NASA grant 80NSSC17K0267 and NSF grant AGS-1759255.

References

Arcodia, M. C., Kirtman, B. P., & Siqueira, L. S. P. (2020). How MJO teleconnections and ENSO interference impacts U.S. precipitation. *Journal of Climate*, *33*(11), 4621–4640. https://doi.org/10.1175/JCLI-D-19-0448.1

Gottschalck, J., Roundy, P. E., Iii, C. J. S., Vintzileos, A., & Zhang, C. (2013). Large-scale atmospheric and oceanic conditions during the 2011–12 DYNAMO field campaign. *Monthly Weather Review*, *141*(12), 4173–4196. https://doi.org/10.1175/MWR-D-13-00022.1

Henderson, S. A., Maloney, E. D., & Barnes, E. A. (2016). The influence of the Madden–Julian oscillation on northern hemisphere winter blocking. *Journal of Climate*, *29*(12), 4597–4616. https://doi.org/10.1175/JCLI-D-15-0502.1

Hoffmann, C. G., Kiladis, G. N., Gehne, M., & Savigny, C. V. (2021). A Python package to calculate the OLR-based index of the Madden–Julian-oscillation (OMI) in climate science and weather forecasting. *Journal of Open Research Software*, *9*(1), 9. https://doi.org/10.5334/jors.331

Jiang, X., Adames, A. F., Kim, D., Maloney, E. D., Lin, H., Kim, H., et al. (2020). Fifty years of research on the Madden-Julian oscillation: Recent progress, challenges, and perspectives. *Journal of Geophysical Research: Atmospheres*, *125*(17), e2019JD030911. https://doi.org/10.1029/2019JD030911

Johnson, R. H., & Ciesielski, P. E. (2013). Structure and properties of Madden–Julian oscillations deduced from DYNAMO sounding arrays. *Journal of the Atmospheric Sciences*, *70*(10), 3157–3179. https://doi.org/10.1175/JAS-D-13-065.1

Jolliffe, I. T. (1995). Rotation of principal components: Choice of normalization constraints. *Journal of Applied Statistics*, *22*(1), 29–35. https://doi.org/10.1080/757584395

Kiladis, G. N., Dias, J., Straub, K. H., Wheeler, M. C., Tulich, S. N., Kikuchi, K., et al. (2014). A comparison of OLR and circulation-based indices for tracking the MJO. *Monthly Weather Review*, *142*(5), 1697–1715. https://doi.org/10.1175/MWR-D-13-00301.1

Liebmann, B., & Smith, C. A. (1996). Description of a complete (interpolated) outgoing longwave radiation dataset. *Bulletin of the American Meteorological Society*, *77*(6), 1275–1277. Retrieved from https://www.jstor.org/stable/26233278

Madden, R. A., & Julian, P. R. (1971). Detection of a 40–50 day oscillation in the zonal wind in the tropical Pacific. *Journal of the Atmospheric Sciences*, *28*(5), 702–708. https://doi.org/10.1175/1520-0469(1971)028<0702:doadoi>2.0.co;2

Madden, R. A., & Julian, P. R. (1972). Description of global-scale circulation cells in the tropics with a 40–50 day period. *Journal of the Atmospheric Sciences*, *29*(6), 1109–1123. https://doi.org/10.1175/1520-0469(1972)029<1109:dogscc>2.0.co;2

North, G. R., Bell, T. L., Cahalan, R. F., & Moeng, F. J. (1982). Sampling errors in the estimation of empirical orthogonal functions. *Monthly Weather Review*, *110*(7), 699–706. https://doi.org/10.1175/1520-0493(1982)110<0699:seiteo>2.0.co;2

Roundy, P. E., Schreck, C. J., & Janiga, M. A. (2009). Contributions of convectively coupled equatorial rossby waves and Kelvin waves to the real-time multivariate MJO indices. *Monthly Weather Review*, *137*(1), 469–478. https://doi.org/10.1175/2008MWR2595.1

Straub, K. H. (2013). MJO initiation in the real-time multivariate MJO index. *Journal of Climate*, *26*(4), 1130–1151. https://doi.org/10.1175/JCLI-D-12-00074.1

Wang, J., Kim, H., Kim, D., Henderson, S. A., Stan, C., & Maloney, E. D. (2020). MJO teleconnections over the PNA region in climate models. Part I: Performance- and process-based skill metrics. *Journal of Climate*, *33*(3), 1051–1067. https://doi.org/10.1175/JCLI-D-19-0253.1

Wang, S. (2019). A precipitation-based index for tropical intraseasonal oscillations. *Journal of Climate*, *33*(3), 805–823. https://doi.org/10.1175/JCLI-D-19-0019.1

Wang, S., Martin, Z. K., Sobel, A. H., Tippett, M. K., Dias, J., Kiladis, G. N., et al. (2022). A multivariate index for tropical intraseasonal oscillations based on the seasonally-varying modal structures. *Journal of Geophysical Research: Atmospheres*, *127*(4), e2021JD035961. https://doi.org/10.1029/2021JD035961

Wheeler, M., & Kiladis, G. N. (1999). Convectively coupled equatorial waves: Analysis of clouds and temperature in the wavenumber–frequency domain. *Journal of the Atmospheric Sciences*, *56*(3), 374–399. https://doi.org/10.1175/1520-0469(1999)056<0374:ccewao>2.0.co;2

Wheeler, M. C., & Hendon, H. H. (2004). An all-season real-time multivariate MJO index: Development of an index for monitoring and prediction. *Monthly Weather Review*, *132*(8), 1917–1932. https://doi.org/10.1175/1520-0493(2004)132<1917:aarmmi>2.0.co;2

Wilks, D. S. (2019). *Statistical methods in the atmospheric sciences*. 4th ed., (Vol. 100). Elsevier Academic Press.

Yoneyama, K., Zhang, C., & Long, C. N. (2013). Tracking pulses of the Madden–Julian oscillation. *Bulletin of the American Meteorological Society*, *94*(12), 1871–1891. https://doi.org/10.1175/BAMS-D-12-00157.1

Zhang, C. (2005). Madden-Julian oscillation. *Reviews of Geophysics*, *43*(2), 1–36. https://doi.org/10.1029/2004RG000158